Chapter 10

State-of-the-Art Design Technique of a Single-Channel Pump for Wastewater Treatment

Jin-Hyuk Kim and Young-Seok Choi

Additional information is available at the end of the chapter

http://dx.doi.org/10.5772/intechopen.75171

Abstract

A single-channel pump, which is commonly used for wastewater treatment, with a single-channel impeller can effectively prevent performance reduction or damage caused by foreign substances. However, the design methods for this special type of pump are different and more difficult to realize than those for general pumps. In this chapter, a state-of-the-art design technique for a single-channel pump is introduced for realizing high efficiency and low-fluid-induced vibration. In other words, advanced multidisciplinary design optimization techniques combined with unsteady flow analysis are introduced and discussed in detail to simultaneously improve hydraulic efficiency and reduce flow-induced vibration, considering the impeller-volute interaction of a single-channel pump.

Keywords: single-channel pump, wastewater treatment, hydraulic efficiency, flow-induced vibration, radial force, optimization

1. Introduction

The most common fault in a submerged pump is due to waste clogging. This phenomenon causes not only motor overload but also serious damage to a pump system. Hence, this type of pump requires unique design features for preventing losses in performance due to factors such as waste clogging, damage, and failure, unlike general submerged pumps.

Representative types of submerged pumps for wastewater treatment consist of the crushing type and flow-path-securing type. A crushing-type pump mostly crushes and transfers foreign substances with a disintegrator installed in front of the impeller. However, as such types of pumps require the installation of an additional crusher, large-sized solid particles cannot be

driven perfectly along the flow path. Moreover, it has a complex structure, high cost, low capacity, and frequent replacement cycle. On the other hand, as a single-channel pump is a representative case of a flow-path-securing type, it has different mechanism features compared with general pumps pressurized by multiblades. A single-channel impeller has one free annulus passage and does not have multiple blades. Further, it is driven by the centrifugal force generated from the rotating annulus passage [1]. Therefore, a single-channel pump is very robust, especially against failure and damage due to waste clogging.

Because of these advantages, the demand for single-channel pumps has increased rapidly in recent times in the field of wastewater treatment. Nevertheless, only a few studies have been published on the design of a single-channel pump [1–4]. To the best of the author's knowledge, the lack of studies can be attributed to the difficulties in establishing a theoretical design methodology, manufacturing, and especially, solving the balancing problem related to the fluid-induced vibration between the impeller and volute of a single-channel pump. In fact, because the mass distribution of a single-channel impeller is not rotationally symmetric, it is difficult to stabilize the fluid-induced vibration between the impeller and volute. Furthermore, unsteady radial forces, which rotate at a frequency generally determined by the rotating speed, are generated in the single-channel impeller [5]. These unsteady sources are generated by the interaction between the rotating impeller and volute, and these adversely affect the overall performance of a single-channel pump, especially its life expectancy and durability.

Over the past several years, there has been growing interest on the effects of unsteady dynamic radial forces due to impeller-volute interaction in centrifugal pumps [6–8]. However, no systematic studies on single-channel pumps have yet been attempted, except for several concepts and patents. To this end, this work presents a state-of-the-art design technique for a single-channel pump for wastewater treatment based on a theoretical approach and three-dimensional steady and unsteady numerical analyses. Moreover, advanced multidisciplinary numerical design optimization techniques are introduced and discussed in detail to simultaneously improve hydraulic efficiency and reduce the flow-induced vibration due to the impeller-volute interaction in a single-channel pump. The objective of this chapter is to provide practical guidelines for optimizing the design of a single-channel pump with the proposed design approach.

2. Basic design approach of single-channel pump

The single-channel pump with an impeller and a volute for wastewater treatment is initially designed according to the Stepanoff theory [9]. The pump can then be modeled as a three-dimensional shape, as shown in **Figure 1** [10]. The three-dimensional model can be developed using commercial modeling software such as SOLIDWORKS and CATIA. Because the Stepanoff theory generally minimizes the flow loss due to flow speed differences by increasing the cross-sectional area of internal flow at a fixed rate according to the theta angle position, it is especially useful for designing a stationary volute. Nonetheless, the impeller of a single-channel pump can be designed based on this concept because it has a free annulus passage

http://dx.doi.org/10.5772/intechopen.75171

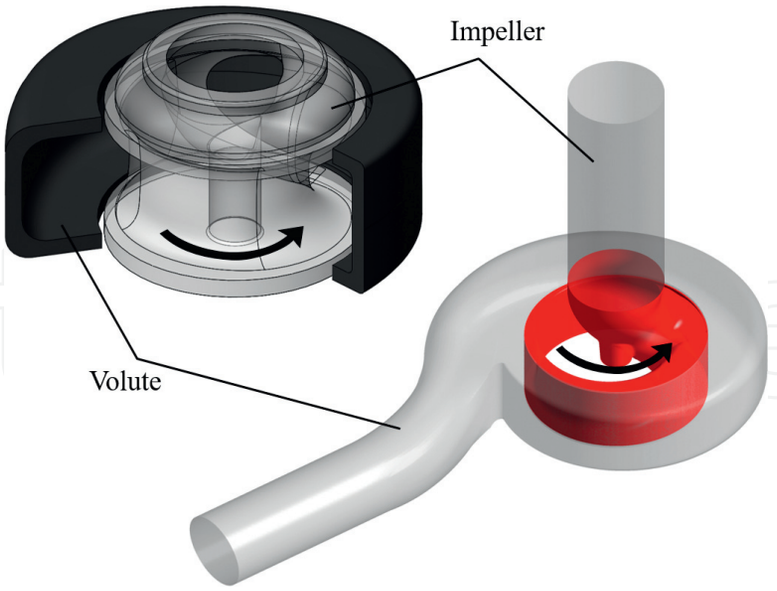

Figure 1. Three-dimensional shape of a single-channel pump [10].

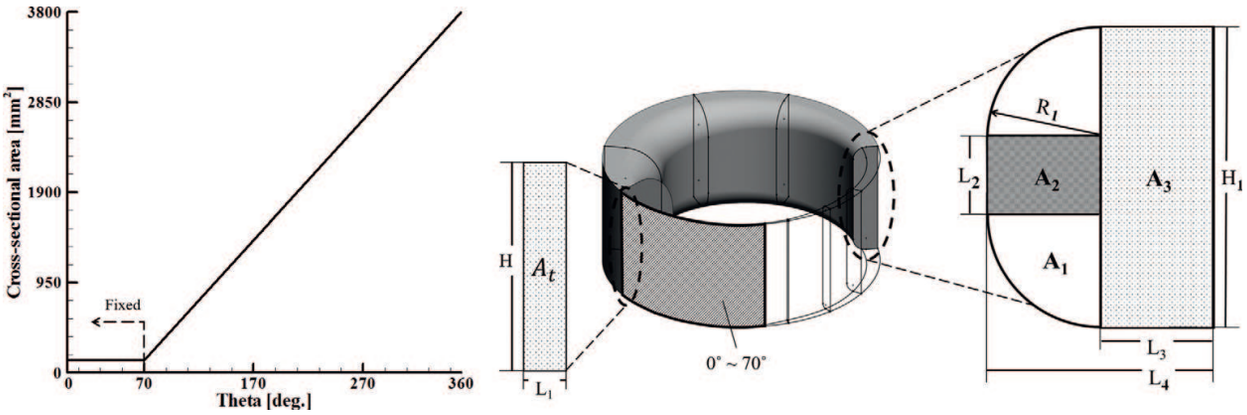

Figure 2. Cross-sectional area distribution and definition of the impeller [10].

and does not contain multiple blades. Further, the impeller is driven by the centrifugal force generated from the rotating annulus passage. Thus, the internal flow distribution in the cross-sectional area of the impeller and volute is changed proportionally with the theta angle position in order to maintain a constant flow velocity. **Figures 2** and **3** show the distribution of internal flows in the cross-sectional area of the impeller and volute generated from the Stepanoff theory. In the authors' previous work, for example, the reference volume flow rate and total head at the design point were 1.42 m^3/min and 10 m, respectively, with a rotational speed of 1760 rpm [11].

When the distribution of internal flows in the cross-sectional area is determined according to the theta angle, the shape of the area should be defined. This shape is very important for deciding the hydraulic performance and size of solid matter in a single channel. In the previous work, the authors proposed a novel design method for defining the cross section of the

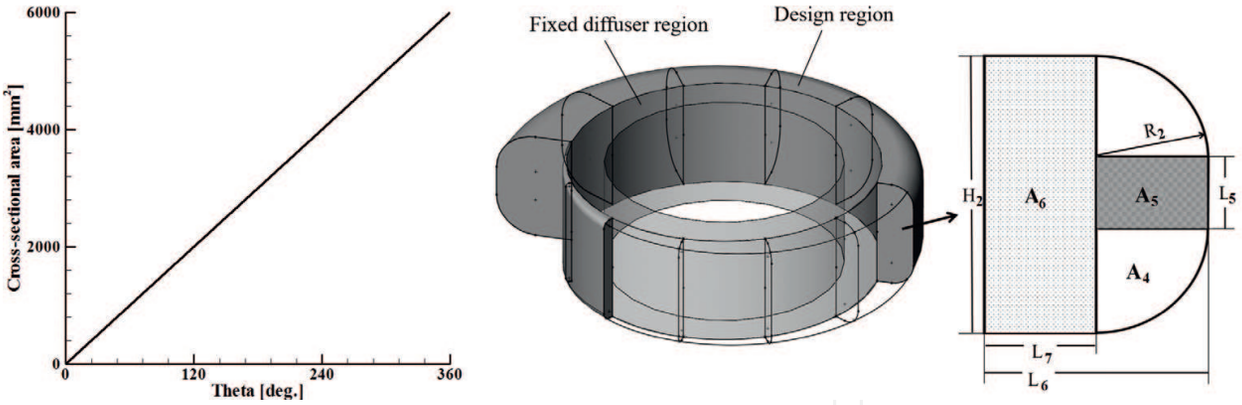

Figure 3. Cross-sectional area distribution and definition of the volute [10].

impeller and volute of a single-channel pump with high performance, as shown in **Figures 2** and **3**, respectively. The cross-sectional area is determined as follows:

The given total area (A_t) in the impeller part,

$$H_1 = 0.835 \times D_1 \tag{1}$$

where the impeller height (H_1) is fixed along theta angle and D_1 represents the inlet diameter of the impeller.

$$A_t\left(@0^\circ \sim 70^\circ\right) = 0.013 \times {D_1}^2 \tag{2}$$

$$L_1 = A_t/H_1 \tag{3}$$

$$A_t\left(@360^\circ\right) = 0.38 \times {D_1}^2 \tag{4}$$

$$A_t = 2A_1 + A_2 + A_3 \tag{5}$$

$$R_1 = \left\{\text{theta}\left(^\circ\right)\text{–}70\ (\text{value of fixed area angle})\right\} \times C_1\ \left(\text{here}, 70^\circ < \text{theta}\left(^\circ\right) \le 360^\circ\right) \tag{6}$$

where $C_1 = 0.1 \times H_1/83.5$ is the expansion coefficient.

$$A_1 = \pi {R_1}^2/4 \tag{7}$$

$$A_2 = R_1 \times L_2 \tag{8}$$

$$A_3 = A_t\text{–}A_2\text{–}2A_1 \tag{9}$$

$$L_3 = A_3/H_1\ (\text{here}, L_3 > 0) \tag{10}$$

The given total area (A_t) in the volute part,

$$H_2 = 0.01 \times A_t\left(@360^\circ\right) \tag{11}$$

where the volute height (H_2) in fixed along theta angle.

$$A_t = 2A_4 + A_5 + A_6 \tag{12}$$

$$R_2 = \text{theta}(^\circ) \times C_2 \tag{13}$$

where $C_2 = 0.1 \times H_2/89.5$ is the expansion coefficient.

$$A_4 = \pi {R_2}^2/4 \tag{14}$$

$$A_5 = R_2 \times L_5 \tag{15}$$

$$A_6 = A_t - 2A_4 - A_5 \tag{16}$$

$$L_7 = A_6/H_2 \ (\text{here}, L_7 > 0) \tag{17}$$

The cross sections of the impeller and volute are defined as mentioned above. The three-dimensional shape can then be modeled as shown in **Figure 1**. The more detailed explanation can be found in the previous works of the authors [12, 13].

3. Steady and unsteady numerical analyses

In the computation domain generated from the basic design approach, the internal flow field is analyzed by solving three-dimensional steady and unsteady incompressible Reynolds-averaged Navier–Stokes (RANS) equations with a k-ω-based shear stress transport (SST) turbulence model by using a finite volume solver. In this work, the commercial computational fluid dynamics (CFD) code ANSYS CFX 14.5 is used, and ICEM CFD is applied to generate computational meshes for the impeller and volute. The numerical analysis is carried out with boundary conditions, solved, and post-processed using ANSYS CFX-Pre, CFX-Solver, and CFX-Post, respectively.

For the turbulence closure model, the k-ω-based SST model [14] is employed to accurately predict flow separation under an adverse pressure gradient. In this model, the k-ω and k-ε models are applied in the near-wall region and bulk domain, respectively, and a blending function ensures smooth transitions between these two models. The accuracy of the numerical analyses of turbulent flows significantly depends on treating the wall shear stress. In this chapter, the near-wall grid resolution is adjusted to maintain $y+ \leq 2$ to accurately capture the wall shear stress and to implement a low-Reynolds-number SST model.

A tetrahedral grid system is constructed in the computational domain with a prism mesh near the surfaces, as shown in **Figure 4** [15]. The rotating single-channel impeller and the volute domains are each constructed using approximately 1,300,000 and 1,200,000 grid points. Hence, the optimum grid system selected using the grid independency test has approximately 2,500,000 grid points, as previously reported [15, 16].

For the boundary condition, water is considered as the working fluid, and the total pressure and designed mass flow rate are set to the inlet and outlet of the computational domain, respectively. The solid surfaces in the computational domain are considered to be hydraulically smooth under

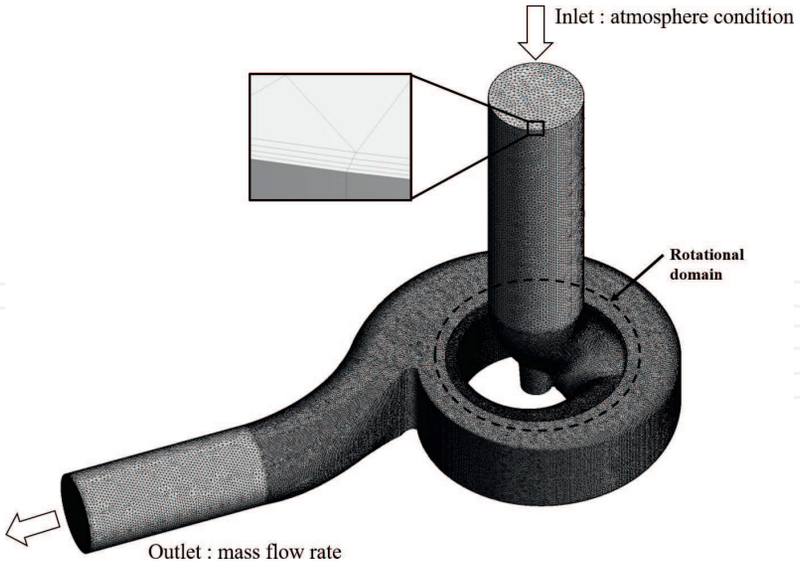

Figure 4. Computational domain and grids.

adiabatic and no-slip conditions. The stage average and transient-rotor-stator methods are respectively applied to connect the interface between the rotating impeller and volute domains in the steady and unsteady analyses.

The convergence criteria in a steady computation consist of the root-mean-square (RMS) values of the residuals of the governing equations, which are set to less than 10^{-5} for all equations. The physical time scale was set to $1/\omega$, where ω is the angular velocity of the impeller. The computations are carried out using an Intel Xeon CPU with a clock speed of 2.70 GHz, and the converged solutions are obtained after 1000 iterations with a computational time of approximately 4 h.

The results of the steady RANS analysis are used in the unsteady RANS analysis to obtain the characteristics of the radial force sources in the region of the exit surface of the impeller according to the impeller-volute interaction in the single-channel pump. In an unsteady simulation, the time step and coefficient loop for the time scale control are set to 0.000947 s and three times, respectively. The solutions are obtained after 180 iterations with an unsteady total time duration of 0.170478 s (five revolutions), and the computational time for the unsteady calculation was approximately 8 h.

4. Optimization techniques

In this chapter, the geometric parameters related to the internal flow through the cross-sectional area of the impeller and volute are selected as design variables to simultaneously optimize the hydraulic efficiency and radial force sources, considering the interaction between the rotating impeller and volute of the single-channel pump. The distribution of internal flow in the cross-sectional area of the impeller and volute can be changed smoothly by adjusting the control points represented by third-order and fourth-order Bezier-curves, respectively, as shown in **Figure 5**. Therefore, the variations in the y-axes for five control points (CP1, CP2,

CP3, CP4, and CP5) of both the impeller and volute are selected as design variables to obtain the most sensitive results for the variation in curve among the control points [17].

The aim of the current optimization problem is to simultaneously improve the hydraulic efficiency (η) and reduce the radial force sources considering the impeller-volute interaction in the single-channel pump. Here, one of the three objective functions, that is, the hydraulic efficiency, is defined as follows.

$$\eta = \frac{\rho g H Q}{\tau \omega} \tag{18}$$

where ρ, g, H, Q, τ, and ω denote the density, acceleration of gravity, total head, volume flow arte, torque, and angular velocity, respectively.

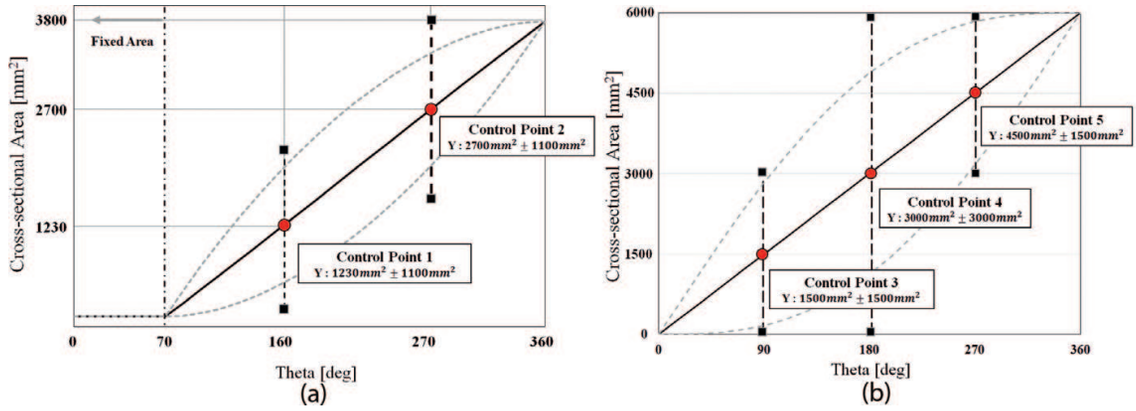

Figure 5. Definition of the design variables. (a) Impeller part (b) Volute part.

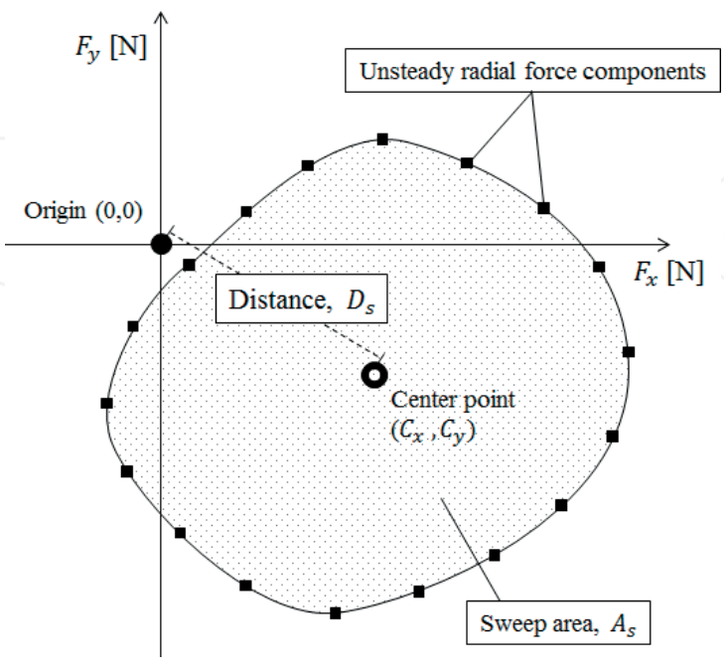

Figure 6. Definition of objective functions related to the radial force sources [10].

The other objective functions related to the radial force sources are defined as the sweep area (As) of the radial force during one revolution of impeller and the distance (Ds) of the mass center of the sweep area from the origin, as shown in **Figure 6**. These functions are defined as follows:

$$A_s = \frac{1}{2}\sum_{i=0}^{n-1}\left(x_i y_{i+1} - x_{i+1} y_i\right) \tag{19}$$

where A_s is the signed area of the polygon as the sweep area of the radial force during one revolution of impeller. The centroid of a non-self-intersecting closed polygon, defined by n vertices (x_0, y_0), (x_1, y_1), …, (x_{n-1}, y_{n-1}), is defined as the point (C_x, C_y) as follows:

$$C_x = \frac{1}{6A_s}\sum_{i=0}^{n-1}\left(x_i + x_{i+1}\right)\left(x_i y_{i+1} - x_{i+1} y_i\right) \tag{20}$$

$$C_y = \frac{1}{6A_s}\sum_{i=0}^{n-1}\left(y_i + y_{i+1}\right)\left(x_i y_{i+1} - x_{i+1} y_i\right) \tag{21}$$

In these formulas, the vertices are assumed to be numbered in the order of their occurrence along the perimeter of the polygon. Therefore, the distance of the mass center of the sweep area from the origin is finally defined as follows:

$$D_s = \sqrt{{C_x}^2 + {C_y}^2} \tag{22}$$

The Latin hypercube sampling (LHS) is employed to generate 54 design points that are used as the initial base data for constructing the response surface from five design variables. LHS, as an effective sampling method for designing and analyzing computer experiments (DACE) [18], is a matrix of order $i \times j$, where i is the number of levels to be examined and j is the number of design variables. Each of the j columns of the matrix containing levels 1, 2, …, i is randomly paired. LHS generates random sample points, ensuring that all portions of the design space are represented. Finally, the objective function values at these design points are evaluated by steady and unsteady numerical analyses.

The response surface approximation (RSA) model is applied as a surrogate model to predict the objective function values based on the 54 design points generated in the design space by using LHS. The RSA model, as a methodology of fitting a polynomial function to discrete responses obtained from numerical calculations, represents the association between the design variables and response functions [19]. The construction function for a second-order polynomial RSA can be expressed as follows:

$$f(x) = \beta_0 + \sum_{j=1}^{N}\beta_j x_j + \sum_{j=1}^{N}\beta_{jj} x_j^2 + \sum\sum_{i\neq j}^{N}\beta_{ij} x_i x_j \tag{23}$$

where β, N, and x represent the regression analysis coefficients, number of design variables, and a set of design variables, respectively, and the number of regression analysis coefficients (β_0, β_i, etc.) is $[(N + 1) \times (N + 2)]/2$.

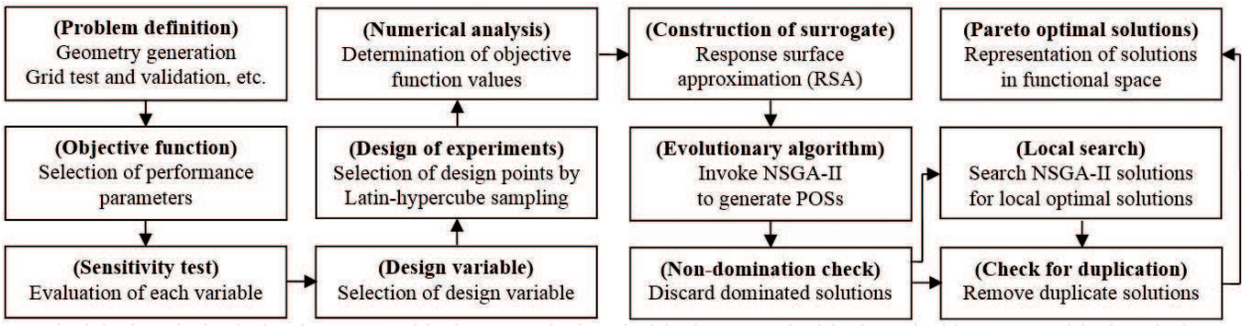

Figure 7. Multiobjective optimization procedure [22].

The RSA models are employed to construct the response surfaces based on the objective function values at the 54 design points generated in the design space using LHS. A hybrid multiobjective genetic algorithm (MOGA) is used to obtain the global Pareto-optimal solutions (POSs). The approximate POSs are obtained using a controlled elitist genetic algorithm (a variant of NSGA-II [20] as the MOGA function for three objective functions. The optimization algorithm and functions in the MATLAB OPTIMIZATION TOOLBOX [21] are used to finally generate the global POSs. **Figure 7** shows an example of the multiobjective optimization procedure [22]. The detailed optimization procedure can be referred to in the previous literatures [23, 24].

5. Results of multiobjective optimization

A hybrid MOGA based on the response surface constructed from the RSA model is employed to obtain the global POSs by using a controlled elitist genetic algorithm (a variant of NSGA-II) for three objective functions. **Figure 8** shows the three-dimensional POSs based on the three objective functions obtained using a hybrid MOGA combined with the RSA model. Here, the values of all the objective function are normalized according to the corresponding values in the reference design. Three-dimensional POSs are obviously the trade-off among the conflicting objective functions. As a result, a trade-off analysis shows an obvious correlation between the hydraulic efficiency and radial force sources. The arbitrary optimum design (AOD) is randomly extracted near the end of the POSs, which exhibits the best performance in terms of all objective functions, as shown in **Figure 8**. The AOD has objective function values that are remarkably improved relative to those in the reference design. Consequently, the value of each objective function in the AOD shows improvements of approximately 49%, 80%, and 4% in the sweep area (As) of the radial force during one revolution, the distance (Ds) of the mass center of the sweep, and the hydraulic efficiency (η), respectively, in comparison with the reference design. On the other hand, a relatively large error among the three objective functions is observed, especially for the distance of the mass center of the sweep. Nevertheless, the values obtained by the numerical analysis are better compared with the reference design.

To understand the optimization results, the trade-off of the POSs in each two-dimensional functional space is shown in **Figure 9**. As shown in **Figure 9(a)** and **(b)**, the decrement in the distance of the mass center of the sweep clearly leads to deterioration in the other objective

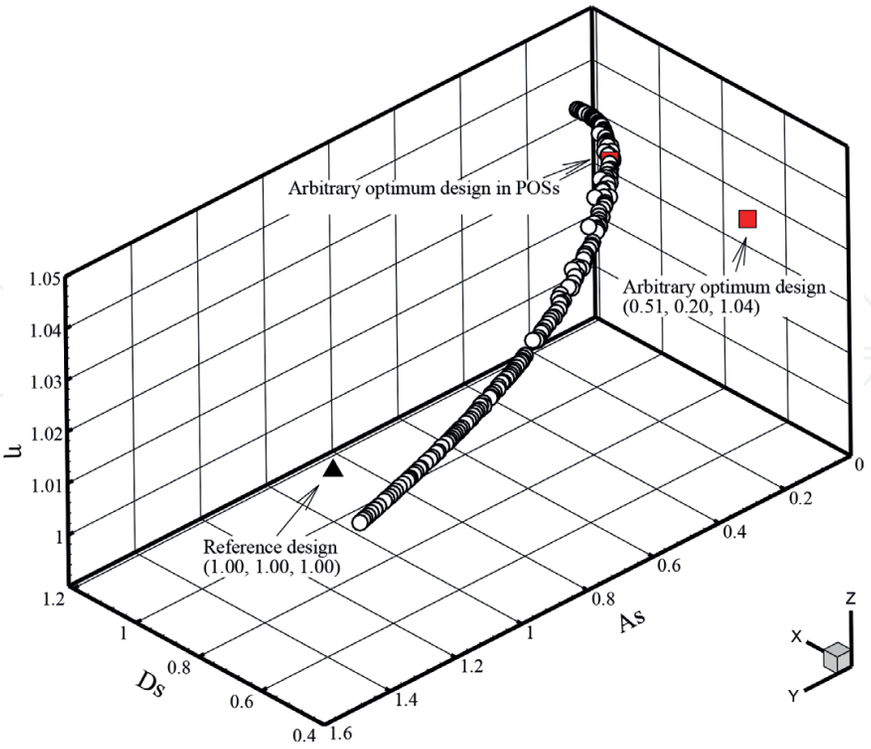

Figure 8. Three-dimensional POSs based on three objective functions. (a) ds-as (b) ds-eff. (c) as-eff.

functions. Specifically, the reduced distance of the mass center of the sweep is obtained at a lower efficiency and higher sweep area of the radial force during one revolution. However, the efficiency and sweep area of the radial force during one revolution shows a positive relation, as shown in **Figure 9(c)**. The trade-off analysis of the POSs therefore allows an engineering designer to choose any economic solution according to the required design conditions.

Figure 10 shows the isosurfaces having a low velocity of 2 m/s. As shown in **Figure 10(a)**, an extremely low-velocity region is formed along the internal wall in the impeller flow path in the reference design, whereas a similar low velocity isosurface is reduced considerably in the arbitrary optimum model (**Figure 10(b)**). These results illustrate the enhancement of hydraulic efficiency in the arbitrary optimum model as a result of optimization.

Figure 11 shows the distributions of unsteady radial force sources, averaged at the boundary surface near the impeller outlet, during one revolution of the impeller for both the reference and AODs. Here, both values are normalized by the value of the maximum radial force in the reference design. The sweep area constructed from the unsteady radial force sources in the reference design leans slightly toward the four quadrant directions from the origin, whereas it is formed near the origin in the AOD. Furthermore, the sweep area in the AOD is remarkably decreased compared with that in the reference design. Consequentially, as discussed already, the sweep area and the distance of the mass center of the sweep in the AOD are decreased by 49% and 80%, respectively, compared with those in the reference design.

Figure 12 shows the unsteady fluctuations of the net radial forces for the reference and AODs during one revolution. Both values are also normalized by the maximum value in the reference

http://dx.doi.org/10.5772/intechopen.75171

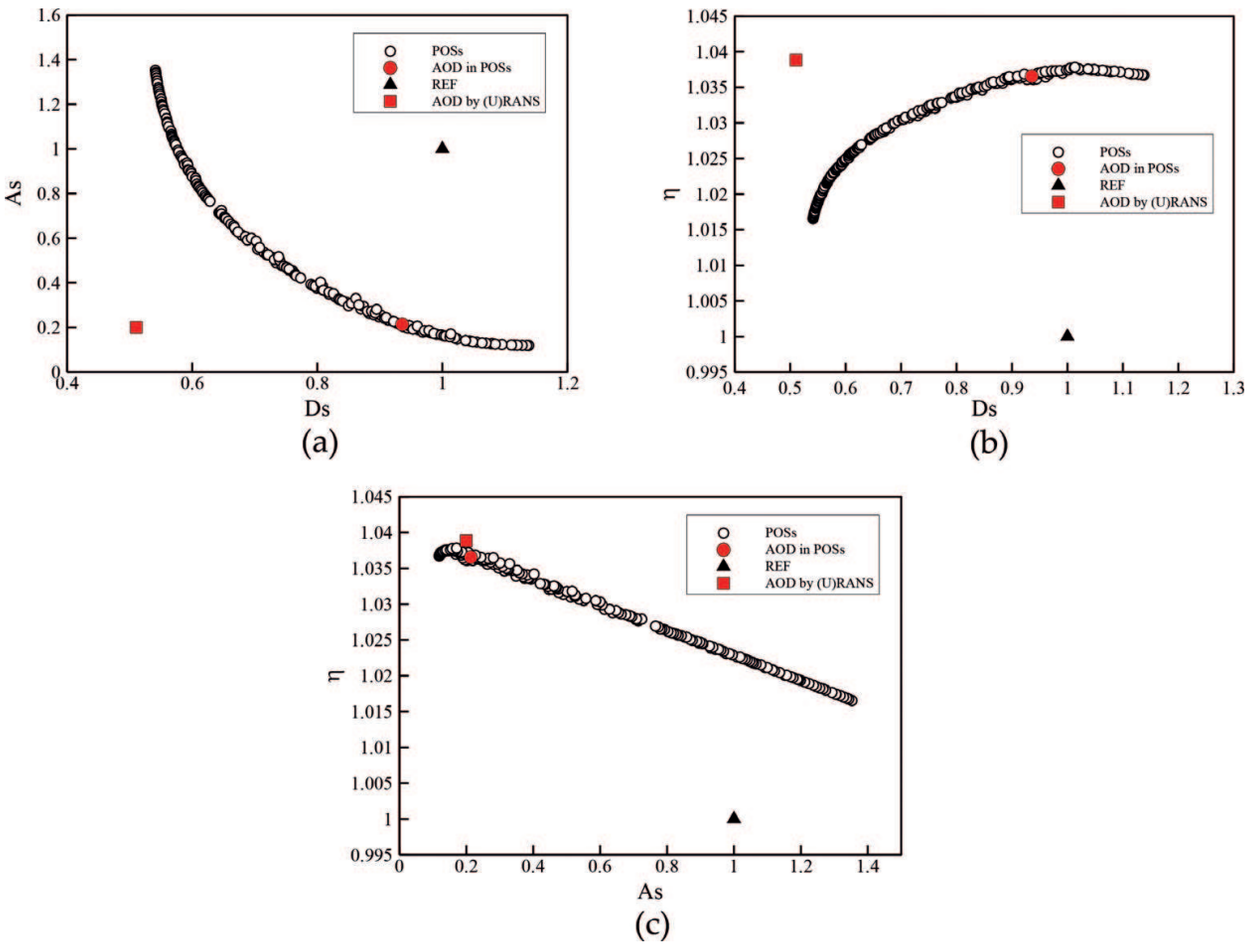

Figure 9. POSs on two-dimensional functional space.

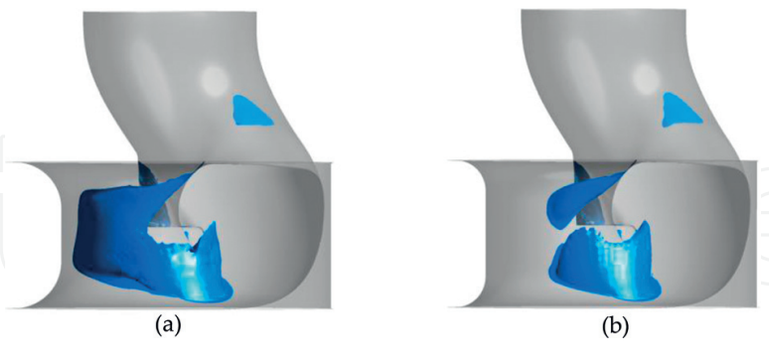

Figure 10. Isosurfaces having a low velocity of 2 m/s. (a) Reference design (b) Arbitrary optimum design.

design. As shown in **Figure 12**, the amplitude values of the fluctuation of the net radial forces in the AOD decrease considerably for most theta angle positions, especially in the region where the value of theta is 100°. In addition, its level is also less than the normalized value of 0.5 and mostly flat compared with the reference design. These phenomena clearly highlight the considerable decrease in the radial force sources as a result of optimization.

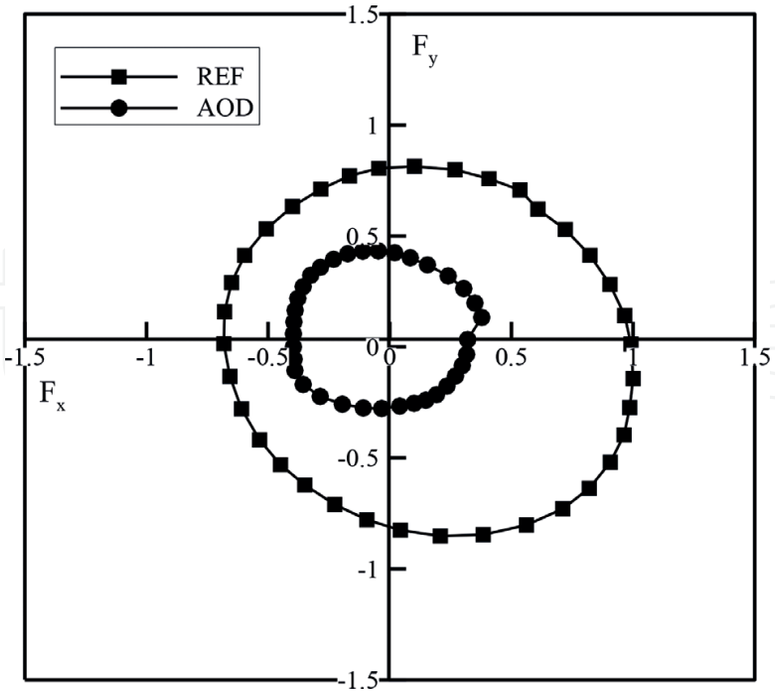

Figure 11. Unsteady radial force distributions during one revolution of the impeller.

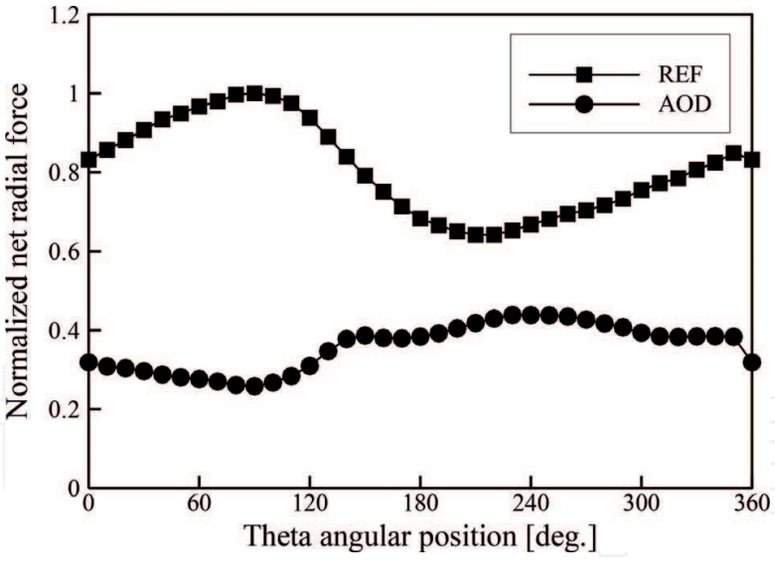

Figure 12. Unsteady net radial force fluctuations during one revolution of the impeller.

Figure 13 shows the time history of instantaneous unsteady pressure contours at the boundary surface near the impeller outlet for both the reference and AODs. Here, both values are normalized by the maximum pressure value in the pressure contours. Both the instantaneous unsteady pressure contours are compared for one rotation τ of the single-channel pump impeller. This rotation is divided into six steps to clarify changes in flow structure with time during one revolution of the impeller, as shown in **Figure 13**. In the reference design, high-pressure zones occur widely on the boundary surface near the impeller outlet, as shown in

http://dx.doi.org/10.5772/intechopen.75171

(a) T = 1/6τ

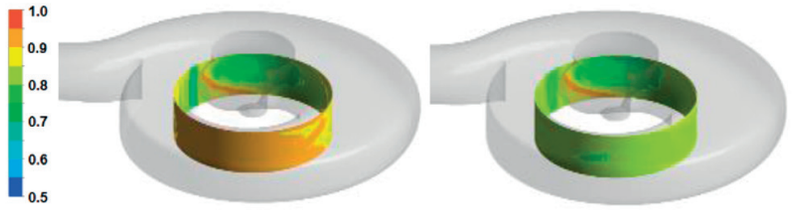

(b) T = 2/6τ

(c) T = 3/6τ

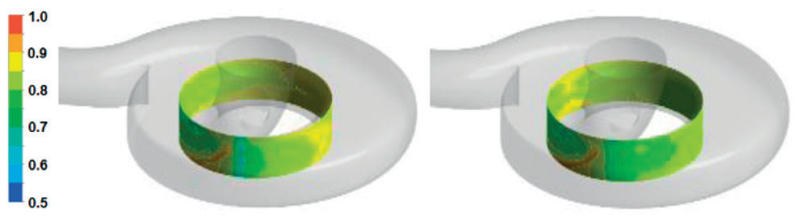

(d) T = 4/6τ

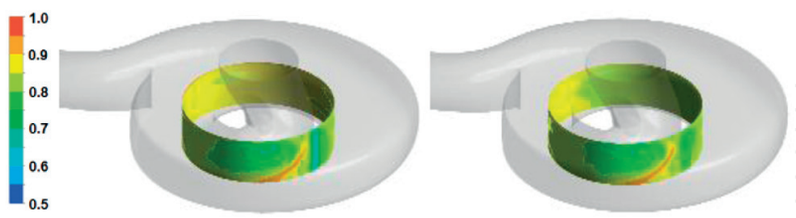

(e) T = 5/6τ

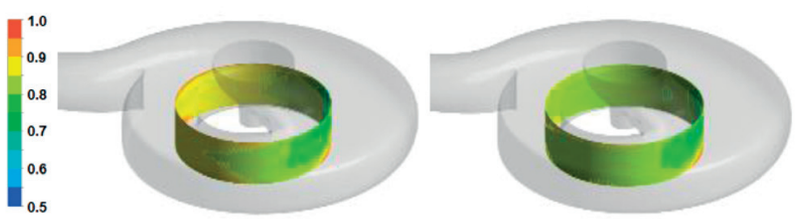

(f) T = 6/6τ

Figure 13. Unsteady pressure contours during one revolution of the impeller. (a) T = 1/6τ. (b) T = 2/6τ. (c) T = 3/6τ. (d) T = 4/6τ. (e) T = 5/6τ. (f) T = 6/6τ.

Figure 13(b), and a high-pressure zone caused by impeller-volute interactions becomes gradually larger. Consequently, this results in the unbalancing phenomena, along with the fluid-induced vibrations caused by unsteady radial forces, throughout the annulus passage area of the pump. Thus, the sweep area constructed from the unsteady radial force sources leans slightly toward the four quadrant directions from the origin, as shown in **Figure 11**. In the AOD, the pressure distribution is generally uniform; especially, at the same instantaneous time, the large high-pressure zone caused by impeller-volute interactions is obviously

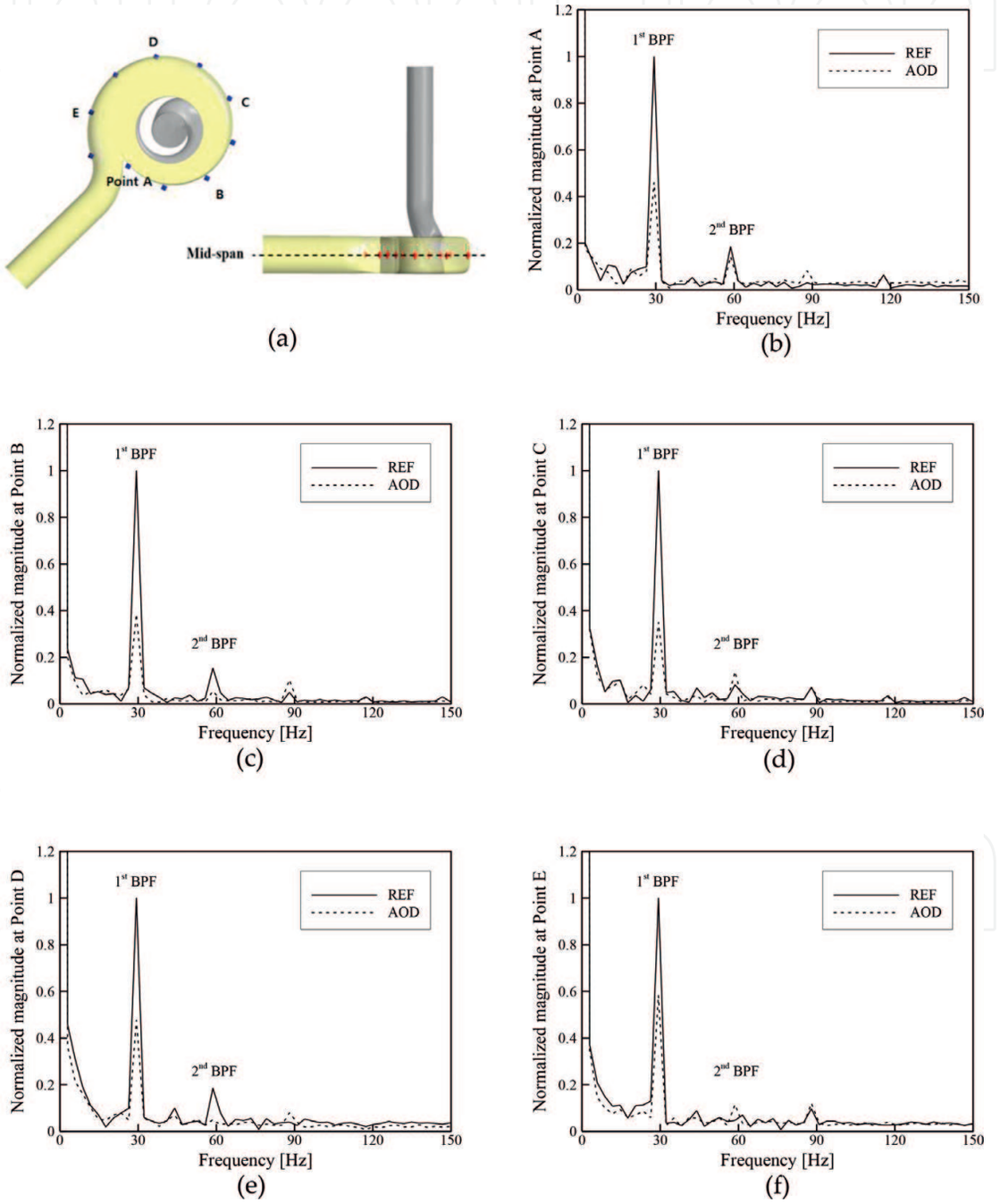

Figure 14. Spectra of the magnitude values at observation points on the casing wall. (a) Location of the observation points (b) Point A. (c) Point B. (d) Point C. (e) Point D. (f) Point E.

suppressed, as shown in **Figure 13(b)**. The AOD results in mostly stable flows throughout the annulus passage area of the pump. This explains the considerable decrease in the fluid-induced vibration caused by impeller-volute interaction owing to optimization.

Figure 14 shows the spectra of the magnitude values at observation points on the casing wall for the reference and AODs. Here, the spectra are calculated based on the wall pressure fluctuation time history by using a fast Fourier transformation algorithm. Both magnitude values are normalized by the first blade passing frequency (BPF) in the reference design, and these values are also related to the vibration of pump. As shown in **Figure 14**, the BPF is approximately 30 Hz (BPF = Blade number $\times$ rpm/60). The peak magnitude values are clearly seen at every harmonic BPF in steps of 30 Hz, which are due to the periodic motion of pump impeller rotation. In the AOD, a considerable decrease in the magnitude values at the first BPF is observed specifically, as well as at all observation points, especially for points B and C. It clearly shows that the large high-pressure zone caused by impeller-volute interactions is obviously suppressed, as shown in **Figure 13(b)**. Consequently, the considerable decreases in these magnitude values reduce the vibration caused by impeller-volute interaction.

6. Conclusions

A state-of-the-art design technique was introduced for a single-channel pump for realizing both high efficiency and low-fluid-induced vibration. The technique is based on a theoretical approach and three-dimensional steady and unsteady numerical analyses. Furthermore, advanced multidisciplinary numerical design optimization techniques were discussed in detail to simultaneously improve hydraulic efficiency and reduce the flow-induced vibration caused by impeller-volute interaction in the single-channel pump. The CFD studies conducted in the last decades, along with an increase in computing power systems, have significantly contributed to the development of various turbomachines with a deep understanding of flow physics and mechanism. Of course, it was possible to suggest a state-of-the-art design technique for a single-channel pump because of the rapid increase in the computing power system and development of computational methods. The authors expect that the practical design technique introduced in this chapter will be useful for engineers designing various single-channel pumps in the near future.

Acknowledgements

This work was supported by the Demand-based-Manufacturing Technique Commercialization R&D Project of the Korea Institute of Industrial Technology (KITECH) (No. JB180001), which was funded by the Ministry of Science and ICT (MSIT). The authors wish to express gratefully our thanks to Ms. Bo-Min Cho (former master student in UST and currently CFD engineer in Anflux Co., Ltd., Korea) and Mr. Wang-Gi Song (currently master student in UST) for their cooperation in the numerical simulation.

Conflict of interest

The author(s) declare no potential conflicts of interest with respect to the research, authorship, and/or publication of this article.

Author details

Jin-Hyuk Kim[1,2]* and Young-Seok Choi[1,2]

*Address all correspondence to: jinhyuk@kitech.re.kr

1 Korea Institute of Industrial Technology (KITECH), Cheonan, Republic of Korea

2 University of Science and Technology (UST), Daejeon, Republic of Korea

References

[1] Hansen BF, Henning PJ. Waste water pump. US patent application no. 13. 2013;**886**:479

[2] Zhang H, Chen B, Shi WD, Pan ZY, Cao WD. Effects of contraction-type impeller on non-overloaded performance for low-specific-speed sewage pump. Journal of Mechanical Science and Technology. 2014;**28**(3):937-944

[3] Pei J, Benra FK, Dohmen HJ. Application of different strategies of partitioned fluid–structure interaction simulation for a single-blade pump impeller. Proceedings of the Institution of Mechanical Engineers, Part E: Journal of Process Mechanical Engineering. 2012;**226**(4):297-308

[4] Keays J, Meskell C. A study of the behaviour of a single-bladed waste-water pump. Proceedings of the Institution of Mechanical Engineers, Part E: Journal of Process Mechanical Engineering. 2006;**220**(2):79-87

[5] Gulich JF. Centrifugal pumps. 2nd ed. Berlin: Spring-Verlag; 2008. pp. 548-549

[6] Gonzalez J, Fernandez J, Blanco E, Santolaria C. Numerical simulation of the dynamic effects due to impeller-volute interaction in a centrifugal pump. Transactions of the ASME—Journal of Fluids Engineering. 2002;**124**:348-355

[7] Gonzalez J, Parrondo J, Santolaria C, Blanco E. Steady and unsteady radial forces for a centrifugal pump with impeller to tongue gap variation. Transactions of the ASME—Journal of Fluids Engineering. 2006;**128**:454-462

[8] Baun DO, Köstner L, Flack RD. Effect of relative impeller-to-volute position on hydraulic efficiency and static radial force distribution in a circular volute centrifugal pump. Transactions of the ASME—Journal of Fluids Engineering. 2000;**121**:598-605

[9] Kelder JDH, Dijkers RJH, Van Esch BPM, Kruyt NP. Experimental and theoretical study of the flow in the volute of a low specific-speed pump. Fluid Dynamics Research. 2001;**28**(4):267-280

[10] Cho BM. A study on numerical optimization of flow path cross-sectional area to improve the hydraulic performance of a single-channel pump [thesis]. Daejeon, Republic of Korea, University of Science and Technology; 2017

[11] Kim JH, Cho BM, Kim YS, Choi YS, Kim KY, Kim JH, Cho Y. Optimization of a single-channel pump impeller for wastewater treatment. International Journal of Fluid Machinery and Systems. 2016;**9**(4):370-381

[12] Kim JH, Choi YS, Lee KY, Cho BM. Single channel pump impeller and centrifugal pump having the same. Korea patent application no. 10–2016-0115198. 2016

[13] Kim JH, Choi YS, Lee KY, Cho BM. Single channel pump volute and centrifugal pump having the same. Korea patent registration no. 10–1784561. 2017

[14] Menter FR. Two-equation eddy-viscosity turbulence models for engineering application. AIAA Journal. 1994;**32**(8):1598-1605

[15] Kim JH, Cho BM, Choi YS, Lee KY. Multi-objective optimization based on unsteady analysis considering the efficiency and radial force of a single-channel pump for wastewater treatment. Journal of Mechanics Engineering and Automation. 2016;**6**:234-245

[16] Kim JH, Cho BM, Choi YS, Lee KY, Peck JH, Kim SC. Optimized reduction of unsteady radial forces in a single-channel pump for wastewater treatment. IOP Conf. Series: Earth and Environmental Science. 2016;**49**:032008

[17] Cho BM, Kim JH, Choi YS, Kim JW, Kim YS, Kim KY, Ahn TS, Kim JH. Surrogate based optimization of a single-channel pump impeller. Proceedings of the 7th International Conference on Pumps and Fans 2015 (ICPF 2015); 18–21 October; Hangzhou. China: 2015. ICPF-121

[18] Sacks J, Welch WJ, Mitchell TJ, Wynn HP. Design and analysis of computer experiments. Statistical Science. 1989;**4**(4):409-435

[19] Myers RH, Montgomery DC. Response Surface Methodology: Process and Product Optimization Using Designed Experiments. New York, USA: Wiley; 1995

[20] Deb K. Multi-Objective Optimization Using Evolutionary Algorithms. 1st ed. Chichester, England, UK: John Wiley & Sons Inc; 2001

[21] MATLAB®. The language of technical computing. Release 14. The Math Work Inc; 2004

[22] Kim JH, Kim JW, Kim KY. Axial-flow ventilation fan design through multi-objective optimization to enhance aerodynamic performance. Transactions of the ASME—Journal of Fluids Engineering. 2011;**133**:101101

[23] Afzal A, Kim KY. Three-objective optimization of a staggered herringbone micromixer. Sensors and Actuators B: Chemical. 2014;**192**:350-360

[24] Shim HS, Afzal A, Kim KY, Jeong HS. Three-objective optimization of a centrifugal pump with double volute to minimize radial thrust at off-design conditions. Proceedings of the Institution of Mechanical Engineers, Part A: Journal of Power and Energy. 2016;**230**(6): 598-615

IntechOpen